Hybrid plasma simulations of the solar wind interaction with an anthropogenic lunar exosphere

A.R. Poppe [a,*], P. Prem [b], S. Fatemi [c], R.M. Killen [d]

[a] *Space Sciences Laboratory, University of California, Berkeley, 7 Gauss Way, Berkeley, CA 94720, USA*
[b] *Applied Physics Laboratory, Johns Hopkins University, 11100 Johns Hopkins Rd., Laurel, MD 20723, USA*
[c] *Dept. of Physics, Umeå University, Umeå 901 87, Sweden*
[d] *NASA Goddard Space Flight Center, Mail Code 695, Greenbelt, MD 20771, USA*

Abstract

In the coming decades, exploration of the lunar surface is likely to increase as multiple nations execute ambitious lunar exploration programs. Among several environmental effects of such activities, increasing traffic near and on the lunar surface will result in the injection of anthropogenic neutral gases into the lunar exosphere. The subsequent ionization of such anthropogenic neutrals in the lunar environment may contribute to and ultimately exceed the generation of 'native' lunar pickup ions, thereby altering the fundamental space plasma interaction with the Moon. To better understand these possible effects, we conducted plasma simulations of the solar wind interaction with the Moon in the presence of increasing ion production rates from an anthropogenic lunar exosphere. At ionization levels between 0.1 and 10 times the native lunar exospheric ion production rate, little to no changes to the solar wind interaction to the Moon are present; however, ionization levels of 100 and 1000 times the native rate result in significant mass loading of the solar wind and disruption of the present-day structure of the Moon's plasma environment. Comparing to the planned Artemis landings, which are likely to contribute only an additional ∼10% of the native lunar exospheric ion production rate, we conclude that the Artemis program will have little effect on the Moon's plasma environment. However, more frequent landings and/or continual outgassing from human settlements on the Moon in the more distant future are likely to fundamentally alter the lunar plasma environment.

1. Introduction

As our nearest celestial neighbor, the Moon presents a key stepping stone as humanity seeks to extend our reach into space. In the past ∼15 years, multiple new missions have contributed to a modern 'lunar renaissance' across many fields of scientific study (e.g., Vondrak et al., 2010; Halekas et al., 2011; Lucey et al., 2022). Looking forward, many nations are planning ambitious robotic and/or human lunar exploration programs, chief among which is NASA's Artemis program, which plans a series of orbital and landed missions over the next decade (e.g., Smith et al., 2020). More broadly, a nascent 'lunar economy' has also been the focus of significant academic and commercial interest (e.g., Crawford, 2015; Utrilla, 2017; Sowers, 2016; Sowers and Dreyer, 2019; Sowers, 2021). In turn, the possibility of a vigorous and sustained presence on the Moon–whether robotic or human–implies a number of potential environmental effects. One such effect is the

---

injection of neutral material at or near the lunar surface from either rocket outgassing during landings or takeoffs or, perhaps eventually, from outgassing of temporary or permanent lunar habitats. Anthropogenically introduced gaseous material has implications for the composition and structure of the lunar exosphere (e.g., Prem et al., 2020) and the accumulation and/or contamination of lunar polar volatile deposits (e.g., Shipley et al., 2015; Witze, 2021).

In its native state, the Moon possesses a tenuous atmosphere composed of dozens of atomic and molecular species originating from multiple sources, including internal outgassing, recycling of solar wind species, charged-particle sputtering, micrometeoroid impact vaporization, and photon-stimulated desorption (e.g., Stern, 1999; Killen and Ip, 1999; Sarantos et al., 2012; Grava et al., 2015; Colaprete et al., 2016; Hurley et al., 2017). The lunar atmosphere is exceedingly tenuous with maximum surface densities of $\sim 10^4 - 10^5$ cm^{-3} and individual particles are essentially collisionless–thus qualifying as an 'exosphere'. In turn, the lunar exosphere responds strongly to external driving functions that govern both source and loss processes. Exospheric sources include the incident charged particle flux for both sputtering and solar-wind recycling (e.g., Potter et al., 2000; Wilson et al., 2006; Benna et al., 2015; Killen et al., 2012; Killen et al., 2021) and meteoroid impact fluxes (e.g., Smith et al., 1999; Szalay et al., 2016; Colaprete et al., 2016). Exospheric losses include direct Jeans escape from hot neutral distributions, recycling to the lunar surface, and ionization and pickup into the ambient plasma flow whether in the form of the solar wind or the terrestrial magnetotail (e.g., Mall et al., 1998; Yokota et al., 2009; Halekas et al., 2012; Halekas et al., 2016; Poppe et al., 2012; Poppe et al., 2022; Shen et al., 2023). The ion production rate from the native lunar exosphere has a maximum of $\sim 10^{-2}$ ions cm^{-3} s^{-1} (Poppe et al., 2022), low enough that while in the solar wind, newly born ions are efficiently picked up into the background flow with little-to-no perturbation to the ambient plasma interaction (e.g., Halekas et al., 2012). The weak nature of this interaction allows the solar wind essentially full access to the lunar surface notwithstanding any local perturbations from lunar crustal magnetic anomalies (e.g., Lin et al., 1998; Halekas et al., 2006; Fatemi et al., 2014). This influx of solar wind drives multiple processes at the lunar surface, including electrostatic surface charging (e.g., Poppe and Horányi, 2010; Stubbs et al., 2014), production of exospheric neutrals via sputtering (e.g., Wurz et al., 2007; Wurz et al., 2022), implantation of protons as part of the formation of surficial OH/H_2O (e.g., Schaible and Baragiola, 2014; Jones et al., 2018; Tang et al., 2021), and the reflection of solar wind particles as energetic neutral atoms (ENAs) (e.g., McComas et al., 2009; Wieser et al., 2009; Szabo et al., 2023). Thus, any changes in the influx of solar wind ions to the lunar surface could impact many other processes in the lunar environment.

In addition to a wealth of studies on the native lunar exosphere, previous work has explored the nature of temporarily induced atmospheres arising from robotic exploration of the lunar surface (e.g., Milford and Pomilla, 1967; Hurley et al., 2014; Shipley et al., 2015; Prem et al., 2020; Farrell et al., 2022). Using a Direct Simulation Monte Carlo (DSMC) approach, Prem et al. (2020) quantified the behavior of a temporary water–vapor exosphere introduced by the landing of a robotic spacecraft on the lunar surface, similar to that of the Chinese Chang'e 3 mission (Liu et al., 2014). The total amount of water injected in this scenario was estimated as ~ 43 kg, or $\sim 1.4 \times 10^{27}$ H_2O molecules. The simulation results showed that while the initial injection of material is local to the landing zone, the volatile nature of the rocket exhaust allows for broad migration over nearly the entire lunar surface. Local water–vapor densities near the landing site initially exceed $\sim 10^5$ cm^{-3}, but the globally distributed average density on the lunar dayside is much lower at $\sim 10^2 - 10^3$ cm^{-3}. At the end of only two lunations (2×29.5 d $= 59$ d), nearly 70% of the injected material has been photo-destroyed, yet $\sim 20\%$ remains temporarily adsorbed to the lunar surface and $\sim 10\%$ has been permanently adsorbed within lunar permanently shadowed regions. The amount of material instantaneously aloft and directly contributing to the exosphere drops from an initial $\sim 3\%$ to $\sim 0.3\%$, and presumably continues to drop as photo-destruction and loss to the polar regions erodes the induced exosphere. While the total amount of material injected into the lunar exosphere and the subsequently induced exospheric densities in the Prem et al. (2020) study were relatively small compared to the estimated native lunar exosphere, these simulations nevertheless demonstrated that local injections of material have global reach across the lunar surface. Thus, the production of an anthropogenic lunar atmosphere–whether from robotic or human activity on the lunar surface–has implications for the plasma interaction of the Moon with its ambient environment. As increasing amounts of anthropogenic material are injected into the Moon's exosphere and subsequently ionized, the Moon's interaction with the solar wind may transition more towards a cometary-like situation where newly born pickup ions are capable to extracting much–if not all–of the solar wind momentum before the solar wind strikes the lunar surface.

Here, we use numerical simulations to study the effects that an anthropogenically induced lunar atmosphere has on the plasma interaction of the Moon with the solar wind, focusing in particular on changes in the near-lunar plasma densities and magnetic fields as well as the flux of solar wind to the lunar surface as a function of anthropogenic neutral densities and associated ionization rates. In Section 2, we describe both the estimates for anthropogenically induced lunar atmospheres and the hybrid plasma model used to investigate the solar wind interaction. In Section 3, we present the results of our simulations, followed by a discussion and conclusion in Section 4.

2. Model description

In the following sections, we describe estimates for the nature of anthropogenically induced lunar exospheres and pickup ionization rates (Section 2.1) and the plasma hybrid model used to investigate the consequences of this ion production source (Section 2.2). We also include a brief discussion of the caveats and limitations of our current investigation in Section 2.3.

2.1. Estimates for anthropogenic exospheres

Table 1 compares estimates for the total propellant mass, equivalent global exospheric water vapor density at the lunar surface, and peak H_2O^+ ion production rate for three potential classes of lunar lander, including (i) a typical robotic lander as part of NASA's Commercial Lunar Payload Services (CLPS) missions, (ii) the 'Starship' Human Landing System (HLS) with the propellant mass estimated for a typical lunar landing, and (iii) the Starship fully loaded to its maximum propellant capacity. These three classes of landers span approximately four orders of magnitude in propellant mass, equivalent global exospheric density at the lunar surface, and H_2O^+ production rate. The surface densities in these three cases span from $\sim 3 \times 10^7$ m^{-3} to $\sim 2 \times 10^{11}$ m^{-3}, or in terms of column density, span from 1.4×10^{12} m^{-2} to 1.0×10^{16} m^{-2} (assuming a mass of 18 amu and a surface temperature of 400 K). For comparison, the typical native lunar exosphere–summed over all species–is estimated to have a total surface density of $\sim 10^{10}$ m^{-3} and a peak ionization rate of $\sim 10^4$ m^{-3} s^{-1} (Poppe et al., 2022). Thus, the CLPS and HLS-class landers are estimated to temporarily inject less neutral and ionized material into the lunar exosphere than the native exosphere (approximately 0.2% and 15% the ionization rate, respectively). In contrast, the fully fueled HLS lander will temporarily inject more material into the lunar exosphere than is natively present by a factor of ~ 20 with an ion production rate higher by a factor of ~ 15. The simulation results of Prem et al. (2020) suggest a characteristic decay time (i.e., the time over which the exosphere will drop by a factor of $1/e$) of ~ 0.86 lunations (~ 25 days) for an induced water–vapor exosphere and thus, the fully fueled HLS water–vapor exosphere should dominate over the native lunar exosphere for approximately 2.6 lunations (~ 76 days).

Due to its presence in rocket exhaust and its general importance in the lunar volatile community, we adopt water vapor (H_2O) as the composition of the induced exosphere, similar to that done in Prem et al. (2020). Furthermore, we assume that this water–vapor exosphere has expanded globally across the lunar surface and is thus isotropic. Investigations with more accurate three-dimensional distributions for the water vapor exosphere are left for future studies. At typical dayside lunar surface temperatures, a thermally accommodated water vapor exosphere should have scale heights of ~ 50–100 km. However, due to computational limits in the hybrid model, the smallest possible grid cell size we are currently able to simulate is 100 km (although we note that future improvements will likely allow higher resolution runs). In order to still resolve the exospheric scale height, we modified the water vapor distribution to have a scale height of 200 km yet reduced the surface density in order to keep the total column density constant. Overall, on the scale of the Moon's interaction with the solar wind, the difference between the 50–100 km and 200 km scale height exosphere is generally negligible for our purposes here. For simplicity, we also assumed that the water vapor scale height was constant across the entire lunar surface.

2.2. Hybrid plasma modeling

In order to simulate the solar wind interaction with the Moon in the presence of an anthropogenic atmosphere, we have used the Amitis hybrid plasma model (Fatemi et al., 2017), which has been previously used to investigate solar wind interactions with the Moon, asteroids, Mercury, and comets (e.g., Fatemi and Poppe, 2018; Fatemi et al., 2020; Rasca et al., 2021; Poppe and Fatemi, 2023; Wang et al., 2023b; Wang et al., 2023a; Gunell et al., 2024). Amitis is a three-dimensional, quasi-neutral hybrid model that employs a Cartesian simulation grid centered at the Moon with the $+x$ axis pointing towards the Sun, the $+z$ axis pointing towards ecliptic north, and the $+y$ axis completing the right-handed set. The Moon is modeled as a spherical object with radius 1750 km (cf. lunar radius of 1738 km) and uniform resistance of 10^7 $\Omega \cdot$m. For this study, we did not include the presence of any crustal magnetic fields. For the ambient plasma conditions, we use a standard solar wind environment with a number density of 5 cm^{-3}, a velocity of 400 km/s in the anti-sunward

Table 1
A comparison of the propellant mass, equivalent global exospheric density, and peak H_2O^+ ion production rate for various sized lunar landers. [1]At the surface, assuming a fraction of 1% aloft in the exosphere globally distributed based on the model results of Prem et al. (2020). [2]Using a H_2O photoionization rate of 7.0×10^{-7} s^{-1} (Huebner and Mukherjee, 2015).

	Propellant Mass [kg]	Equiv. global exospheric density[1] [H_2O/m^3]	H_2O^+ Prod. Rate[2] [m^{-3} s^{-1}]
CLPS-class	160	2.8×10^7	2.0×10^1
Starship (typical)	12,800	2.3×10^9	1.6×10^3
Starship (full)	1,200,000	2.1×10^{11}	1.5×10^5

direction, ion and electron temperatures of 10 eV, and an interplanetary magnetic field of [0.0, +5.0, 0.0] nT. Under these conditions, the convection electric field is 2.0 mV/m, the solar wind dynamic pressure is 1.34 nPa, and the electron and ion inertial lengths are 2.4 and 100 km, respectively. Note that these scales place the simulation firmly in the hybrid regime (e.g., see Fig. 3 of Fatemi et al., 2017) and thus, a magnetohydrodynamic (MHD) approach would be inappropriate in this case. Indeed, as discussed by e.g., Ledvina et al. (2008) and Fatemi et al. (2017), hybrid-kinetic approaches to simulating plasma dynamics is required whenever the relevant ion scales (e.g., inertial lengths, gyroradii) approach or exceed the size of object or region of interest. As discussed below, the inclusion of heavy lunar exospheric pickup ions with gyroradii much greater than the lunar radius thus necessitates a hybrid approach.

In addition to the solar wind, the hybrid model also includes newly ionized H_2O^+ ions from the anthropogenically induced exosphere discussed above in Section 2.1. For simplicity, we assume ionization to only be due to photoionization and thus, only sunlit regions of the exosphere produce H_2O^+ pickup ions. To span a broad range of induced exospheric ionization, we simulated five separate cases each of which increase the ionization rate by one order-of-magnitude. As depicted in Fig. 1, the exospheric ion production rates span from $0.1\times$ the native lunar exospheric ion production rate ('Run 1') to $1000\times$ the native lunar exospheric ion production rate ('Run 5'). In terms of absolute units, this range of simulations spans ionization rates from 10^3 m^{-3} s^{-1} to 10^7 m^{-3} s^{-1}. Fig. 1 also shows the estimated ion production rates for the CLPS, HLS typical, and HLS fully fuelded landers, respectively. The CLPS lander has an ionization rate far below even our lowest simulation, while the typical HLS lander is near our Run 1 with $0.1\times$ the native lunar exospheric ion production rate. The

fully fueled HLS lander has an estimated ion production rate just larger than our Run 3, which is $10\times$ the native lunar exospheric ion production rate. Finally, we note that while our Runs 4 and 5, at $100\times$ and $1000\times$ the native lunar ion production rate, are higher than estimated for individual landers (at least in the near future), we nevertheless explore them to quantify the effects that such extreme ion production rates have on the lunar-solar wind interaction. All hybrid simulations were run at least 75 s, equivalent to approximately two full transit times of the solar wind through the simulation domain, and were determined to have achieved steady state equilibrium by inspection.

2.3. Caveats and limitations

Here, we note and acknowledge certain caveats and/or limitations to our modeling investigation, keeping in mind that our goal in this study is to provide a first look into the effects of anthropogenic outgassing on the solar wind interaction with the Moon rather than an exhaustive characterization of all possible conditions. First, as noted in Section 2.1, we have adopted a relatively simple analytic formulation for the anthropogenic H_2O exosphere and its subsequent ionization into pickup ions. The neutral distribution has been assumed to be isotropic and with constant scale height, which neglects both surface-temperature variations and more complex particle dynamics in a rarified exosphere (e.g., lateral transport, nightside condensation, etc.; Prem et al., 2020). As a first order investigation, such a simplified approach is justified, although we do acknowledge a much broader and more complex range of neutral exosphere models could be implemented to better characterize anisotropies within any anthropogenic water–vapor exosphere at the Moon. Within the hybrid modeling setup, we have explicitly chosen a standard set of solar wind and interplanetary magnetic field conditions; again, our aim is to keep these first simulations relatively straightforward. Similar to the neutral exosphere discussed above, one can envision a suite of additional simulations that characterize the variability in the lunar plasma interaction in the presence of anthropogenic pickup ions over the full range of both solar wind variations at the Moon and as a function of lunar phase as the Moon transits from the solar wind, through the terrestrial magnetotail, and back into the solar wind once per lunation. For example, high levels of anthropogenic pickup ion production at the Moon while the Moon transits the low density terrestrial magnetotail lobes may yield an even more perturbed lunar plasma environment than in the solar wind, as any newly born pickup ions are not as promptly carried away due to the much lower convection speeds in the magnetotail (e.g., Troshichev et al., 1999; Poppe et al., 2012; Cao et al., 2020b; Cao et al., 2020a; Liuzzo et al., 2021). Finally, we also note that we have not included any species from the native lunar exosphere (e.g., see Poppe et al., 2022) in order to simplify the simulation and focus solely on the anthropogenic exospheric effects. One might expect that at high levels of
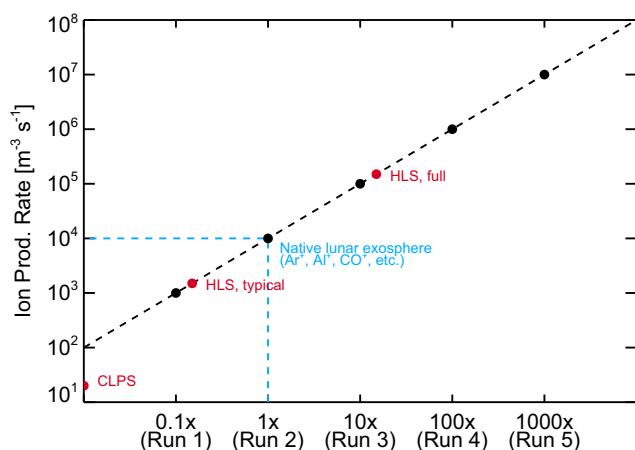

Fig. 1. The peak H_2O^+ ion production rate for each of five runs conducted with the hybrid model (black dots). The estimated ion production from the native lunar exosphere is denoted by the light-blue dashed lines (Poppe et al., 2022) and the estimated peak ion production rates from the CLPS, typical HLS, and fully fueled HLS landers (see Table 1) are denoted as the red dots.

anthropogenic pickup ion production where the Moon's plasma interaction is severely disturbed, the dynamics and recycling of native exospheric pickup ion species may be heavily altered. Again, we leave such investigations to future work.

3. Model results

In the following sections, we describe the results of our simulations as they pertain to the global solar wind interaction with the Moon, Section 3.1, and as they pertain to the solar wind flux to the lunar surface, Section 3.2.

3.1. Global plasma interaction

Fig. 2 shows the solar wind density, ionospheric H_2O^+ density, and total magnetic field strength in the x-z plane

for Runs 1, 2, and 3, respectively. In all three cases, the solar wind density seen in the left-most column are essentially identical. Upstream of and lateral to the Moon, little to no perturbations are evident, while downstream of the Moon, a lunar wake is formed in all three cases due to the absorption of solar wind protons on the upstream hemisphere of the Moon. The lunar wake slowly fills back in with increasing downstream distance, as previously observed and suggested by simulations (e.g., Ogilvie et al., 1996; Halekas et al., 2005; Holmström et al., 2012; Zhang et al., 2014). The distributions of exospheric pickup ions, seen in the middle column of Fig. 2, all display the standard cycloid motion expected for newly picked-up ions (e.g., Hartle and Killen, 2006), as they are accelerated away from the Moon. The dominant "plume" of pickup ions originates from the lunar dayside and $+z$ hemisphere while an additional, lower density plume originates from a small
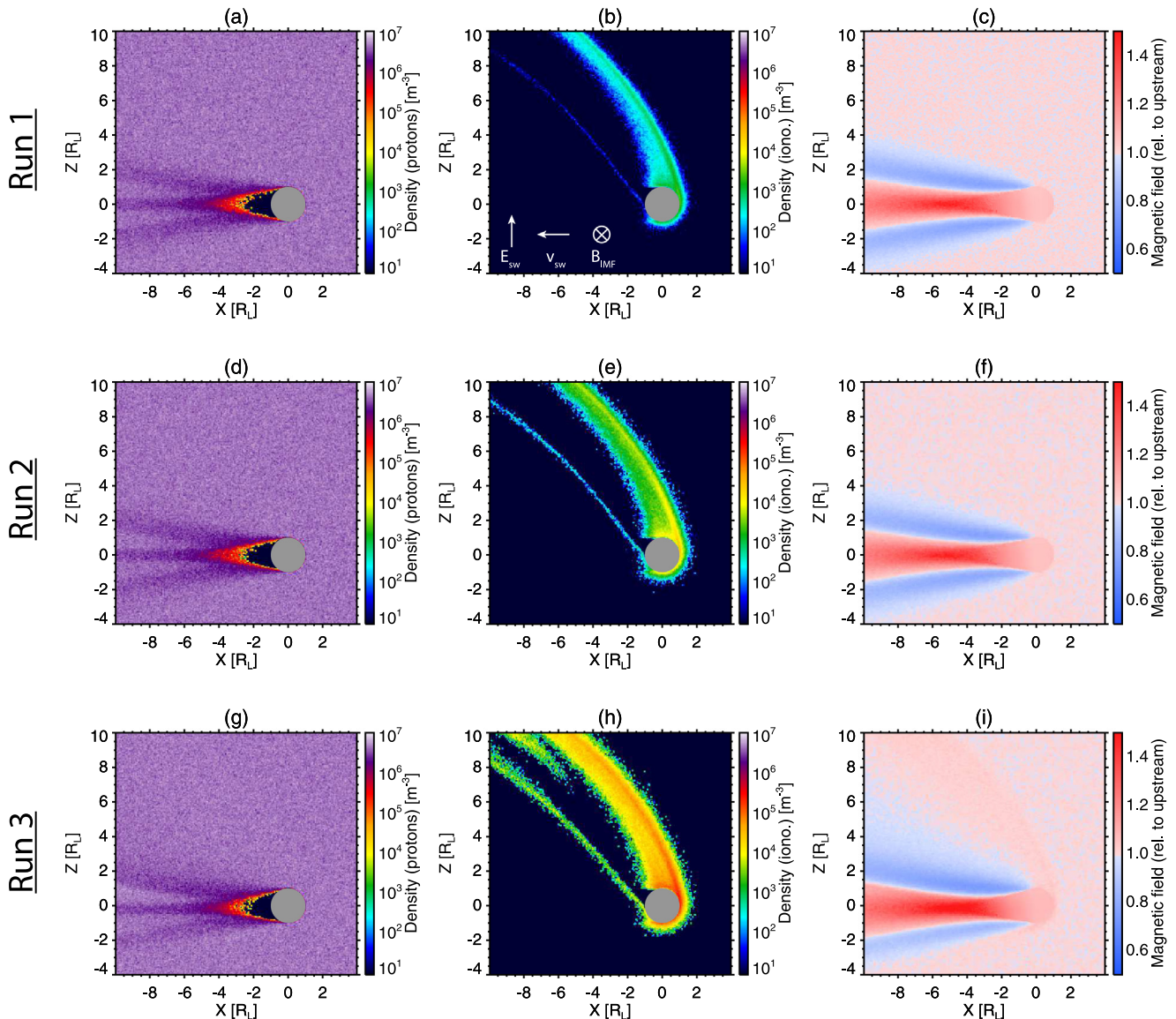

Fig. 2. Hybrid model results for the (left) solar wind proton density, (center) ionospheric H_2O^+ density, and (right) magnetic field magnitude, respectively, in the X-Z plane for Runs 1, 2, and 3. Note that the magnetic field magnitude is normalized to the upstream value. The solar wind velocity, convection electric field, and interplanetary magnetic field vectors are denoted in the lower left of panel (b).

portion of the induced exosphere in the -x/-z hemisphere. Here, a small fraction of newborn pickup ions are able to just avoid striking the lunar surface before transiting through the lunar wake. The overall distribution of exospheric pickup ions generally remains similar as the exospheric density and total ionization rate increases from Run 1 to Run 3, although we do note that in Run 3, there is an additional population of pickup ions that appears in this plane at distances $z > +8$ R_L as some pickup ions drift inwards towards the midplane. Near the sub-solar point at the surface of the Moon, the density of H_2O^+ ions relative to that of the solar wind for these three runs is approximately, $10^{-3}, 10^{-2}$, and 10^{-1}, respectively. Similarly, in all three cases the magnetic field magnitude seen in panels (c), (f), and (i) are nearly identical. In Run 1 and Run 2, no perturbations of the magnetic field strength are seen either upstream of or lateral to the Moon. In Run 3, however, we note both a faint compressional feature co-aligned with the exospheric pickup ion tail and a north–south asymmetry in the rarefaction waves downstream of the Moon. Downstream of the Moon, the formation of the lunar wake induces a series of currents along the wake boundaries (e.g., Fatemi et al., 2013) that induce a central compression in the magnetic field surrounding by a pair of outwardly propagating rarefaction waves (see also Holmström et al., 2012; Vernisse et al., 2013). Only very slight differences in the magnitude of these magnetic features downstream of the Moon are seen in Run 3 compared to Runs 1 and 2.

In comparison, Fig. 3 shows the solar wind proton density, ionospheric H_2O^+ density, and magnetic field magnitude for Runs 4 and 5. With exospheric ion production rates of $100\times$ and $1000\times$ the native lunar exosphere, the solar wind interaction with the Moon is significantly altered. In Run 4, the differences in the solar wind proton density distributions are most apparent downstream of the Moon. The low-density wake behind the Moon is compressed closer to the downstream surface and series of limb compressions are seen originating from the -z hemisphere. The apparent refilling of the lunar wake by solar wind protons at distances $x < -2$ R_L is dictated by conservation of momentum: as the solar wind picks up ionospheric ions in the $+z$ direction, solar wind protons are driven in the opposite direction into the wake. This refilling process is not entirely uniform, thus leaving regions of slightly lower proton densities (dark red regions, $\sim 10^6$ m^{-3}) downstream of the Moon.

The ionospheric H_2O^+ pickup ion density is still roughly cycloidal to first order, yet significantly scattered from the well organized plumes seen in Runs 1 through 3. Downstream of the Moon, the H_2O^+ pickup ion motion has a considerable out-of-plane ($\pm y$) component as ambipolar electric fields due to the density gradient in the wake draws these ions inwards along the magnetic field. At distances between -2 R_L and -4 R_L, these ions cross the midplane from both directions, thus appearing as a density enhancement within the nominal lunar wake. At distances greater than -4 R_L, the H_2O^+ pickup ions continue further along
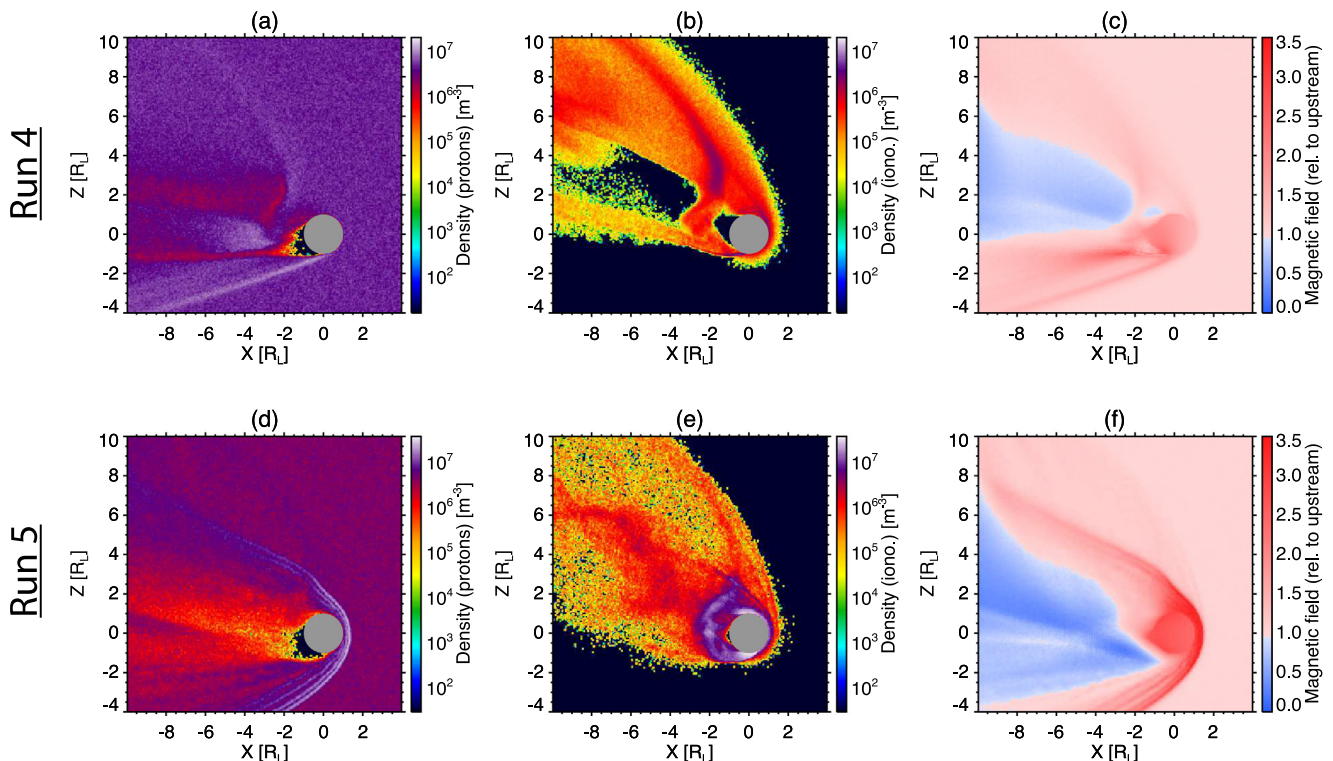

Fig. 3. The hybrid model results for Runs 4 and 5 in the same format as Fig. 2, although note the change in color scale for the magnetic field magnitude.

$\pm y$ and leave the midplane, thus leaving behind a larger low-density void. The interplanetary magnetic field is also highly altered compared to Runs 1–3 with compressions apparent on both the $+z$ and $-z$ hemispheres of the Moon. Additionally, there is a small signature of a magnetic compression immediately above the upstream lunar surface, potentially indicating a weak compression or shock-like feature that is beginning to form.

In Run 5, the Moon's interaction with the solar wind has transitioned to a strongly mass-loaded scenario much more reminiscent of induced magnetosphere interactions such as observed at comets, Mars, Titan, and/or Pluto (e.g., Delamere, 2006; Delamere, 2009; Rubin et al., 2015; Feyerabend et al., 2017; Gunell et al., 2024). As seen in the solar wind proton density, a fully formed bow shock is present upstream of the Moon at a standoff distance of ~1.4 R_L. Downstream of the Moon, a wake is still present, but is significantly broader than in earlier runs. The ionospheric H_2O^+ ion density is primarily concentrated at much lower altitudes above the lunar surface where H_2O^+ densities approach 50 cm^{-3} as the solar wind convection is unable to fully pick the ions up. Only those H_2O^+ ions at

the upper most scale heights of the neutral exospheric distribution are fully picked up and carried away with the solar wind. The interplanetary magnetic field also shows the presence of a bow shock, with a compression of over $3.5\times$ the upstream field strength.

3.2. Solar wind flux to the moon

The flux of solar wind ions to the surface of the Moon plays a critical role in several processes, including neutral exospheric generation via charged-particle sputtering (e.g., Wurz et al., 2007; Wurz et al., 2022), the production of surficial hydroxyl and/or water on lunar regolith via proton implantation (e.g., Schaible and Baragiola, 2014; Jones et al., 2018; Tang et al., 2021), and the formation of space-weathered amorphous rims in lunar regolith (e.g., Christoffersen et al., 1996; Keller and McKay, 1997). Thus, any alteration in the flux of solar wind protons to the lunar surface could change the conditions under which each of these processes operate. Fig. 4(a-e) shows the spatial distribution of solar wind flux to the lunar surface for Runs 1 through 5, in units relative to the upstream,
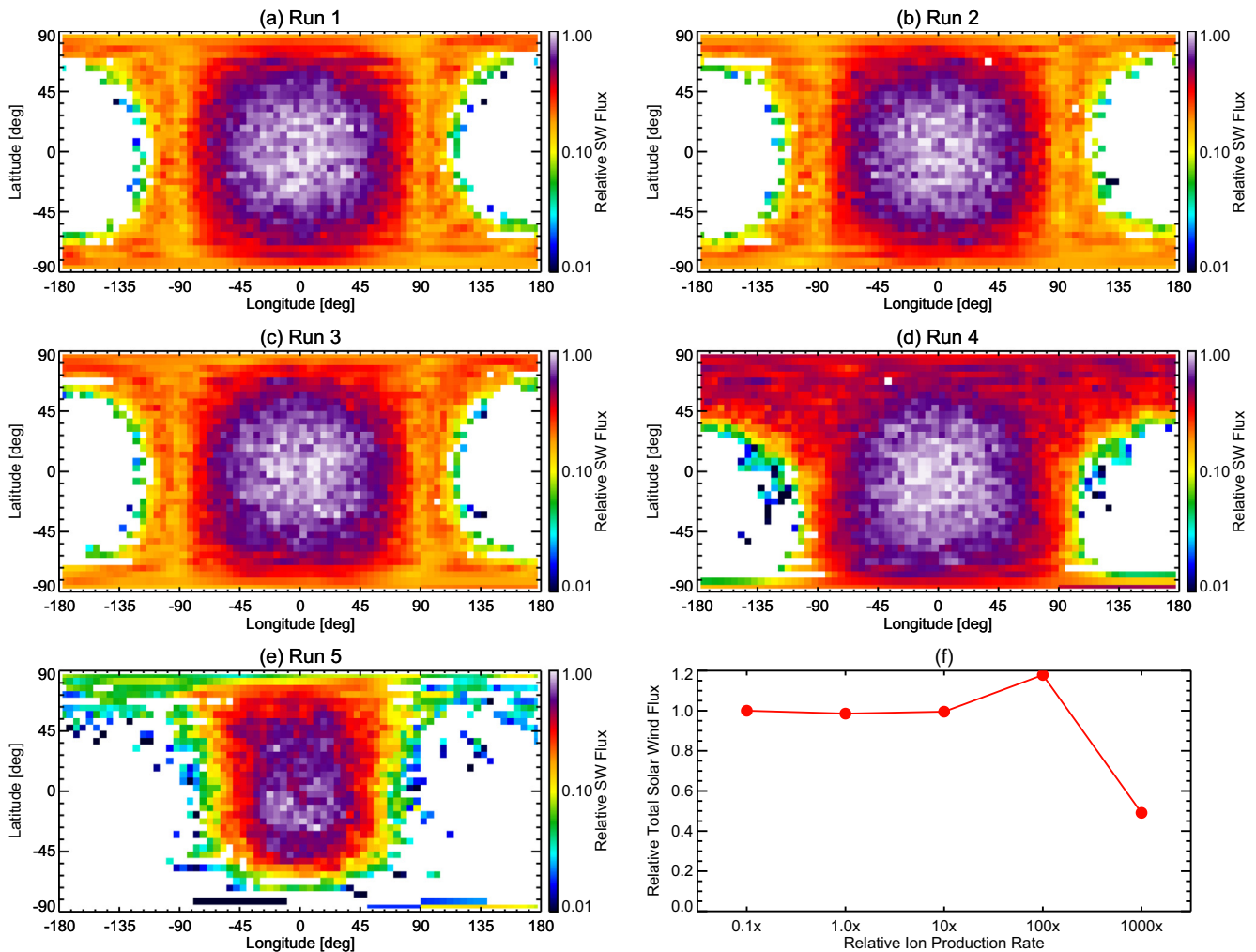

Fig. 4. (a-e) The relative flux of solar wind protons to the lunar surface as a function of lunar longitude and latitude for each of the five runs. (f) The total integrated flux of solar wind protons to the Moon as a function of the relative anthropogenic exospheric ion production rate.

undisturbed solar wind flux, while panel 4(f) shows the globally averaged flux to the lunar surface relative to the upstream flux. In Runs 1, 2, and 3, the solar wind flux to the lunar surface is concentrated on the lunar dayside (longitudes $< \pm 90°$) with an approximate decline as the cosine of the solar zenith angle. The flux of solar wind protons at and just past the terminators continues at decreasing levels before reaching zero flux at solar zenith angles greater than $\approx 110°$ (see also Halekas et al., 2005; Fatemi et al., 2012). All three of these cases share essentially the same characteristics and are indicative of little-to-no change in the solar wind proton flux to the lunar surface relative to present-day conditions.

In contrast, Runs 4 and 5 display notable differences in the solar wind proton flux to the lunar surface. In Run 4, panel 4(d), the flux of solar wind protons to the upstream hemisphere is slightly increased in particular towards the terminators. Additionally, the proton flux is clearly increased in the northern, high-latitudes of the lunar surface, even extending down to $-45°$ on the nightside surface. This increased solar wind proton flux to the northern hemisphere is explained via the momentum transfer from the solar wind protons to the newly born H_2O^+ pickup ions. As the H_2O^+ ions are picked up by the solar wind motional electric field–which in the northern hemisphere, points *away* from the Moon–they extract momentum from the bulk solar wind proton population. In turn, conservation of momentum implies that the solar wind protons must move in the opposite direction, i.e., *towards* the Moon. Incidentally, the same momentum exchange is responsible for the limb compression seen in the *-z* hemisphere for Run 4 (i.e., see panels 3(a) and (c)), although in this hemisphere, the H_2O^+ pickup ions are accelerated into the lunar surface (and quickly reabsorbed) while the solar wind protons are forced away from the Moon. Overall, this momentum exchange between the solar wind protons and the ionospheric H_2O^+ pickup ions *increases* the overall solar wind proton flux to the lunar surface by a factor of $\sim 20\%$, see panel 4(f).

Finally, at an ionospheric production rate of $1000\times$ the native exospheric rate, panel 4(e) shows that the solar wind proton flux to the lunar surface has in fact begun to decrease, although the overall spatial distribution of the solar wind proton flux to the lunar surface is similar to that in Run 4, panel 4(d), with a peak concentration on the dayside and some excess flux in the northern hemisphere (due to the aforementioned momentum exchange with the ionospheric H_2O^+ ions). Nevertheless, as seen in panel 4(f), the total solar wind flux to the lunar surface has dropped by a factor of $\sim 50\%$ relative to the undisturbed case. Additionally, while not shown here, the typical impact speed of the solar wind protons has declined from upstream values of 400 km/s to values of $\sim 150 - 300$ km/s at the surface. Along with the reduction in flux seen in this case, the reduction in the impact velocity has further implications for the efficiency of processes such as charged-particle sputtering and space weathering of grains, as these processes are in general energy dependent. As an example, the combined reduction of $\sim 50\%$ in flux and $\sim 50\%$ in impact speed implies a charged-particle sputtering rate only $\sim 20\%$ that of the undisturbed case.

4. Discussion and conclusion

The simulations presented here are a first step towards understanding the potential impacts that future human exploration of the Moon may have on the lunar plasma environment. At levels anticipated for individual lunar landings for either robotic or human exploration (i.e., the CLPS or HLS 'typical' cases), the additional presence of exospheric H_2O^+ pickup ions has a negligible impact on the overall lunar plasma interaction. In the case of a fully fueled HLS, the total exospheric ion production rate is predicted to exceed the native pickup ion production rate by approximately one order of magnitude; however, even at this level only minor perturbations to the lunar plasma interaction are noted in the simulations. Furthermore, absent a continuous source of anthropogenic gases at this level, this excess contribution is expected to dissipate within approximately two lunations (Prem et al., 2020). That acknowledged, we do also note that such an increase in the exospheric pickup ion rate would be readily detectable by in situ plasma instrumentation at the Moon, as the ARTEMIS mission routinely observes pickup ion flux from the native lunar exosphere (e.g., Halekas et al., 2012; Halekas et al., 2016; Harada et al., 2015).

Anthropogenic gas production in the lunar environment has a much greater impact on the lunar plasma interaction at levels approximately 100 and 1000 times the native lunar exosphere. Our simulations show that at these levels of exospheric ion production, the incident solar wind and interplanetary magnetic field are significantly perturbed. Both of these cases show the presence of plasma compressions and/or fully formed shocks. The outflow of newly produced exospheric ions is heavily stagnated and consequently, ionospheric densities can exceed solar wind densities near the lunar surface. Solar wind fluxes to the lunar surface are also affected by an anthropogenic atmosphere at 100 and 1000 times the native exosphere. The $100\times$ case (Run 4) demonstrates an increase in solar wind flux to the surface due to momentum transfer with the exospheric H_2O^+ ions while the $1000\times$ case (Run 5) demonstrates a $\sim 50\%$ decrease in solar wind flux due to diversion of the solar wind around the ionospheric obstacle. While we have not explicitly modeled such cases, an extrapolation to even higher values of anthropogenic outgassing (e.g., 10^5 times the native exosphere) are likely to continue the trend of increased solar wind mass loading and decreased solar wind flux to the lunar surface. Furthermore, it is worth noting that the effects of anthropogenic outgassing and ionization may be more pronounced in the high-latitude and/or polar regions where ambient densities near the surface from the lunar photoelectron sheath

are naturally lower (e.g., Stubbs et al., 2014). Given the stated interest and plans to land human mission in the lunar polar regions, further investigation into the effects of anthropogenic outgassing at the poles (e.g., Farrell et al., 2024) is clearly warranted.

Putting these results into the broader context of upcoming human exploration of the lunar surface, we conclude that significant human-induced perturbations to the lunar-solar wind interaction are not likely to occur in at least the next decade. The current human exploration plans for NASA's Artemis program call for at most one HLS landing per year (equivalent to Run 1) which is itself ~100 times lower than the level at which our simulations show even minimal perturbations, i.e., Run 3. Furthermore, maintaining such a minimum perturbation would require the landing of a fully fueled HLS on the lunar surface at a cadence of once every one to two months, a pace that far outstrips any current plans. Nevertheless, we do also acknowledge that if a sustained human presence on the lunar surface is someday achieved, a majority of anthropogenically released gases may come from either permanent habitats or industrial-scale mining and/or processing activities rather than from crew or cargo landings. As such habitats and industrial activities are considered, the simulations presented here can provide a reference for anticipated effects on the lunar-solar wind plasma interaction.

Declaration of Competing Interest

The authors declare that they have no known competing financial interests or personal relationships that could have appeared to influence the work reported in this paper.

Acknowledgments

References

Benna, M., Mahaffy, P.R., Halekas, J.S., et al., 2015. Variability of helium, neon, and argon in the lunar exosphere as observed by the LADEE NMS instrument. Geophys. Res. Lett. 42, 3723–3729. https://doi.org/10.1002/2015GL064120.

Cao, X., Halekas, J., Poppe, A. et al., 2020a. The acceleration of lunar ions by magnetic forces in the terrestrial magnetotail lobes. J. Geophys. Res.: Space Physics, 125. doi:10.1029/2020JA027829.

Cao, X., Halekas, J.S., Chu, F., et al., 2020b. Plasma convection in the terrestrial magnetotail lobes measured near the moon's orbit. Geophys. Res. Lett. 47. https://doi.org/10.1029/2020GL090217.

Christoffersen, R., Keller, L.P., McKay, D.S., 1996. Microstructure, chemistry, and origin of grain rims on ilmenite from the lunar soil finest fraction. Meteorit. Planet. Sci. 31, 835–848. https://doi.org/10.1111/j.1945-5100.1996.tb02117.x.

Colaprete, A., Sarantos, M., Wooden, D.H., et al., 2016. How surface composition and meteoroid impacts mediate sodium and potassium in the lunar exosphere. Science 351 (6270), 249–252. https://doi.org/10.1126/science.aad2380.

Crawford, I.A., 2015. Lunar resources: a review. Prog. Phys. Geog.: Earth Env. 39 (2), 137–167. https://doi.org/10.1177/0309133314567585.

Delamere, P.A., 2006. Hybrid code simulations of the solar wind interaction with Comet 19P/Borrelly. J. Geophys. Res. 111 (A12217). https://doi.org/10.1029/2006JA011859.

Delamere, P.A., 2009. Hybrid code simulations of the solar wind interaction with Pluto. J. Geophys. Res. 114 (A03220), 1–17. https://doi.org/10.1029/2008JA013756.

Farrell, W.M., Prem, P., Hurley, D.M., et al., 2024. Possible anthropogenic contributions to the LAMP-observed surficial icy regolith within lunar polar craters: a comparison of apollo and starship landings. Plan. Sci. J. 5 (105). https://doi.org/10.3847/PSJ/ad37f5.

Farrell, W.M., Prem, P., Tucker, O.J., et al., 2022. A lingering local exosphere created by a gas plume of a lunar lander. Icarus 376 (114857). https://doi.org/10.1016/j.icarus.2021.114857.

Fatemi, S., Holmström, M., Futaana, Y., 2012. The effects of lunar surface plasma absorption and solar wind temperature anisotropies on the solar wind proton velocity space distributions in the low-altitude lunar plasma wake. J. Geophys. Res. 117 (A10105). https://doi.org/10.1029/2011JA017353.

Fatemi, S., Holmström, M., Futaana, Y., et al., 2013. The lunar wake current systems. Geophys. Res. Lett. 40, 17–21. https://doi.org/10.1029/2012GL054635.

Fatemi, S., Holmström, M., Futaana, Y., et al., 2014. Effects of protons reflected by lunar crustal magnetic fields on the global lunar plasma environment. J. Geophys. Res.: Space Physics 119, 6095–6105. https://doi.org/10.1002/2014JA019900.

Fatemi, S., Poppe, A.R., 2018. Solar wind plasma interaction with asteroid 16 Psyche: implication for formation theories. Geophys. Res. Lett. 45, 39–48. https://doi.org/10.1002/2017GL073980.

Fatemi, S., Poppe, A.R., Barabash, S., 2020. Hybrid simulations of solar wind proton precipitation to the surface of mercury. J. Geophys. Res.: Space Physics 125. https://doi.org/10.1029/2019JA027706.

Fatemi, S., Poppe, A.R., Delory, G.T., et al., 2017. AMITIS: A 3D GPU-Based Hybrid-PIC model for space and plasma physics. J. Phys.: Conf. Series 837 (012017). https://doi.org/10.1088/1742-6596/837/1/012017.

Feyerabend, M., Liuzzo, L., Simon, S., et al., 2017. A three-dimensional model of pluto's interaction with the solar wind during the new horizons encounter. J. Geophys. Res.: Space Phys. 122, 10356–10368. https://doi.org/10.1002/2017JA024456.

Grava, C., Chaufray, J.-Y., Retherford, K.D., et al., 2015. Lunar exospheric argon modeling. Icarus 255, 135–147. https://doi.org/10.1016/j.icarus.2014.09.029.

Gunell, H., Goetz, C., Fatemi, S., 2024. Impact of radial interplanetary magnetic fields on the inner coma of comet 67P/Churyumov-Gerasimenko: Hybrid simulations of the plasma environment. Astron. Astrophys. 682 (A62). https://doi.org/10.1051/0004-6361/202348186.

Halekas, J.S., Bale, S.D., Mitchell, D.L., et al., 2005. Electrons and magnetic fields in the lunar plasma wake. J. Geophys. Res. 110 (A07222). https://doi.org/10.1029/2004JA010991.

Halekas, J.S., Brain, D.A., Mitchell, D.L., et al., 2006. On the occurrence of magnetic enhancements caused by solar wind interaction with lunar crustal fields. Geophys. Res. Lett. 33 (L08106). https://doi.org/10.1029/2006GL025931.

Halekas, J.S., Poppe, A.R., Delory, G.T., et al., 2012. Lunar pickup ions observed by ARTEMIS: Spatial and temporal distribution and constraints on species and source locations. J. Geophys. Res. 117 (E06006). https://doi.org/10.1029/2012JE004107.

Halekas, J.S., Poppe, A.R., Farrell, W.M., et al., 2016. Structure and composition of the distant lunar exosphere: Constraints from ARTEMIS observations of ion acceleration in time-varying fields. J. Geophys. Res.: Planets 121, 1102–1115. https://doi.org/10.1002/2016JE005082.

Halekas, J.S., Saito, Y., Delory, G.T., et al., 2011. New views of the lunar plasma environment. Planet. Space Sci. 59, 1681–1694. https://doi.org/10.1016/j.pss.2010.08.011.

Harada, Y., Halekas, J.S., Poppe, A.R., et al., 2015. Statistical characterization of the foremoon particle and wave morphology: ARTEMIS observations. J. Geophys. Res.: Space Phys. 120, 4907–4921. https://doi.org/10.1002/2015JA021211.

Hartle, R.E., Killen, R., 2006. Measuring pickup ions to characterize the surfaces and exospheres of planetary bodies: applications to the Moon. Geophys. Res. Lett. 33 (L05201). https://doi.org/10.1029/2005GL024520.

Holmström, M., Fatemi, S., Futaana, Y., et al., 2012. The interaction between the Moon and the solar wind. Earth Planets Space 64, 237–245. https://doi.org/10.5047/eps.2011.06.040.

Huebner, W.F., Mukherjee, J., 2015. Photoionization and photodissociation rates in solar and blackbody radiation fields. Planet. Space Sci. 106, 11–45. https://doi.org/10.1016/j.pss.2014.11.022.

Hurley, D.M., Benna, M., Mahaffy, P.R. et al., 2014. Upper limits on the propagation of constituents of the Chang'e-3 exhaust plume from LADEE observations. In: 45th Annual Lunar and Planetary Science Conf. 1777.

Hurley, D.M., Cook, J.C., Retherford, K.D., et al., 2017. Contributions of solar wind and micrometeoroids to molecular hydrogen in the lunar exosphere. Icarus 283, 31–37. https://doi.org/10.1016/j.icarus.2016.04.019.

Jones, B.M., Aleksandrov, A., Hibbits, K., et al., 2018. Solar wind-induced water cycle on the Moon. Geophys. Res. Lett. 45, 10959–10967. https://doi.org/10.1029/2018GL080008.

Keller, L.P., McKay, D.S., 1997. The nature and origin of rims on lunar soil grains. Geochim. Cosmochim. Acta 61 (11), 2331–2341. https://doi.org/10.1016/S0016-7037(97)00085-9.

Killen, R.M., Hurley, D.M., Farrell, W.M., 2012. The effect on the lunar exosphere of a coronal mass ejection passage. J. Geophys. Res. 117 (E00K02). https://doi.org/10.1029/2011JE004011.

Killen, R.M., Ip, W.-H., 1999. The surface-bounded atmosphere of Mercury and the Moon. Rev. Geophys. 37 (3), 361–406. https://doi.org/10.1029/1999RG900001.

Killen, R.M., Morgan, T.H., Potter, A.E., et al., 2021. Coronagraphic observations of the lunar sodium exosphere 2018–2019. Icarus 355 (114155). https://doi.org/10.1016/j.icarus.2020.114155.

Ledvina, S.A., Ma, Y.-J., Kallio, E., 2008. Modeling and simulating flowing plasmas and related phenomena. Space Sci. Rev. 139, 143–189. https://doi.org/10.1007/s11214-008-9384-6.

Lin, R.P., Mitchell, D.L., Curtis, D.W., et al., 1998. Lunar surface magnetic fields and their interaction with the solar wind: results from lunar prospector. Science 281, 1480–1484. https://doi.org/10.1126/science.281.5382.1480.

Liu, J.J., Yan, W., Li, C.L., et al., 2014. Reconstructing the landing trajectory of the CE-3 lunar probe by using images from the landing camera. Res. Astron. Astrophys. 14 (12), 1530–1542. https://doi.org/10.1088/1674-4527/14/12/003.

Liuzzo, L., Poppe, A.R., Halekas, J.S., et al., 2021. Investigating the Moon's interactions with the terrestrial magnetotail lobe plasma. Geophys. Res. Lett. 48. https://doi.org/10.1029/2021GL093566.

Lucey, P.G., Petro, N., Hurley, D.M., et al., 2022. Volatile interactions with the lunar surface. Geochemistry 82 (125858). https://doi.org/10.1016/j.chemer.2021.125858.

Mall, U., Kirsch, E., Cierpka, K., et al., 1998. Direct observation of lunar pick-up ions near the Moon. Geophys. Res. Lett. 25 (20), 3799–3802. https://doi.org/10.1029/1998GL900003.

McComas, D.J., Allegrini, F., Bochsler, P., et al., 2009. Lunar backscatter and neutralization of the solar wind: First observations of neutral atoms from the Moon. Geophys. Res. Lett. 36. https://doi.org/10.1029/2009GL038794.

Milford, S.N., Pomilla, F.R., 1967. A diffusion model for the propagation of gases in the lunar atmosphere. J. Geophys. Res. 72 (17), 4533–4545. https://doi.org/10.1029/JZ072i017p04533.

Ogilvie, K.W., Steinberg, J.T., Fitzenreiter, R.J., et al., 1996. Observations of the lunar plasma wake from the WIND spacecraft on December 27, 1994. Geophys. Res. Lett. 23 (10), 1255–1258. https://doi.org/10.1029/96GL01069.

Poppe, A., Horányi, M., 2010. Simulations of the photoelectron sheath and dust levitation on the lunar surface. J. Geophys. Res. 115 (A08106). https://doi.org/10.1029/2010JA015286.

Poppe, A.R., Fatemi, S., 2023. The solar wind interaction with (1) Ceres: The role of interior conductivity. Plan. Sci. J. 4 (14). https://doi.org/10.3847/PSJ/acaf6a.

Poppe, A.R., Halekas, J.S., Harada, Y., 2022. A comprehensive model for pickup ion formation at the Moon. J. Geophys. Res.: Planets 127. https://doi.org/10.1029/2022JE007422.

Poppe, A.R., Samad, R., Halekas, J.S., et al., 2012. ARTEMIS observations of lunar pick-up ions in the terrestrial magnetotail. Geophys. Res. Lett. 39 (L17104). https://doi.org/10.1029/2012GL052909.

Potter, A.E., Killen, R.M., Morgan, T.H., 2000. Variation of lunar sodium during passage of the Moon through the Earth's magnetotail. J. Geophys. Res. 105 (E6), 15,073–15,084. https://doi.org/10.1029/1999JE001213.

Prem, P., Hurley, D.M., Goldstein, D.B., et al., 2020. The evolution of a spacecraft-generated lunar exosphere. J. Geophys. Res.: Planets 125. https://doi.org/10.1029/2020JE006464.

Rasca, A.P., Fatemi, S., Farrell, W.M., et al., 2021. A double disturbed lunar plasma wake. J. Geophys. Res.: Space Physics 126. https://doi.org/10.1029/2020JA028789.

Rubin, M., Gombosi, T.I., Hansen, K.C., et al., 2015. Modeled Interaction of Comet 67P/Churyumov-Gerasimenko with the Solar Wind Inside 2 AU. Earth Moon Planets 116, 141–157. https://doi.org/10.1007/s11038-015-9476-8.

Sarantos, M., Killen, R.M., Glenar, D.A., et al., 2012. Metallic species, oxygen and silicon in the lunar exosphere: Upper limits and prospects for LADEE measurements. J. Geophys. Res. 117 (A03103). https://doi.org/10.1029/2011JA017044.

Schaible, M.J., Baragiola, R.A., 2014. Hydrogen implantation in silicates: The role of solar wind SiOH bond formation on the surfaces of airless bodies in space. J. Geophys. Res.: Planets 119, 2017–2028. https://doi.org/10.1002/2014JE00465.

Shen, H.-W., Halekas, J.S., Poppe, A.R., 2023. Limits on the density of the lunar ionosphere: ARTEMIS Observations. Astrophys. J. 958 (165). https://doi.org/10.3847/1538-4357/ad054b.

Shipley, S.T., Metzger, P.T., Lane, J.E., 2015. Lunar Cold Trap Contamination by Landing Vehicles. In: L.S. Gertsch, & R.B. Malla (Eds.), Earth and Space 2014. ASCE. doi:10.1061/9780784479179.018.

Smith, M., Craig, D., Herrmann, N., et al., 2020. The Artemis Program: An Overview of NASA's Activities to Return Humans to the Moon. In: In 2020 IEEE Aerospace Conference, pp. 1–10. https://doi.org/10.1109/AERO47225.2020.9172323.

Smith, S.M., Wilson, J.K., Baumgardner, J., et al., 1999. Discovery of the distant lunar sodium tail and its enhancement following the Leonid Meteor Shower of 1998. Geophys. Res. Lett. 26 (12), 1649–1652. https://doi.org/10.1029/1999GL900314.

Sowers, G.F., 2016. A cislunar transportation system fueled by lunar resources. Space Policy 37–2, 103–109. https://doi.org/10.1016/j.spacepol.2016.07.004.

Sowers, G.F., 2021. The business case for lunar ice mining. New Space 9 (2). https://doi.org/10.1089/space.2020.0045.

Sowers, G.F., Dreyer, C.B., 2019. Ice mining in lunar permanently shadowed regions. New Space 7 (4), 235–244. https://doi.org/10.1089/space.2019.0002.

Stern, S.A., 1999. The lunar atmosphere: history, status, current problems, and context. Rev. Geophys. 37 (4), 453–491. https://doi.org/10.1029/1999RG900005.

Stubbs, T.J., Farrell, W.M., Halekas, J.S., et al., 2014. Dependence of lunar surface charging on solar wind plasma conditions and solar irradiation. Planet. Space Sci. 90, 10–27. https://doi.org/10.1016/j.pss.2013.07.008.

Szabo, P.S., Poppe, A.R., Mutzke, A., et al., 2023. Energetic Neutral Atom (ENA) emission characteristics at the moon and mercury from 3d regolith simulations of solar wind reflection. J. Geophys. Res.: Planets 128. https://doi.org/10.1029/2023JE007911.

Szalay, J.R., Horányi, M., Colaprete, A., et al., 2016. Meteoritic influence on sodium and potassium abundance in the lunar exosphere measured by LADEE. Geophys. Res. Lett. 43, 6096–6102. https://doi.org/10.1002/2016GL069541.

Tang, H., Li, X., Zeng, X., et al., 2021. Experimental investigation of structural OH/H_2O in different lunar minerals and glass via solar-wind proton implantation. Icarus 359 (114322). https://doi.org/10.1016/j.icarus.2021.114322.

Troshichev, O., Kokubun, S., Kamide, Y., et al., 1999. Convection in the distant magnetotail under extremely quiet and weakly disturbed conditions. J. Geophys. Res. 104 (A5), 10249–10263. https://doi.org/10.1029/1998JA900141.

Utrilla, C.M.E., 2017. Establishing a framework for studying the emerging cislunar economy. Acta Astronaut. 141, 209–218. https://doi.org/10.1016/j.actaastro.2017.10.005.

Vernisse, Y., Kriegel, H., Wiehle, S., et al., 2013. Stellar winds and planetary bodies simulations: Lunar type interaction in super-Alfvénic and sub-Alfvénic flows. Planet. Space Sci. 84, 37–47. https://doi.org/10.1016/j.pss.2013.04.004.

Vondrak, R., Keller, J., Chin, G., et al., 2010. Lunar Reconnaissance Orbiter (LRO): Observations for Lunar Exploration and Science. Space Sci. Rev. 150, 7–22. https://doi.org/10.1007/s11214-010-9631-5.

Wang, X.-D., Fatemi, S., Holmström, M., et al., 2023a. Martian global current systems and related solar wind energy transfer: hybrid simulations under nominal conditions. Mon. Not. R. Astron. Soc. 527 (4), 12232–12242. https://doi.org/10.1093/mnras/stad3486.

Wang, X.-D., Fatemi, S., Nilsson, H., et al., 2023b. Solar wind interaction with Mars: electric field morphology and source terms. Mon. Not. R. Astron. Soc. 521 (3), 3597–3607. https://doi.org/10.1093/mnras/stad247.

Wieser, M., Barabash, S., Futaana, Y., et al., 2009. Extremely high reflection of solar wind protons as neutral hydrogen atoms from regolith in space. Planet. Space Sci. 57, 2132–2134. https://doi.org/10.1016/j.pss.2009.09.012.

Wilson, J.K., Mendillo, M., Spence, H.E., 2006. Magnetospheric influence on the Moon's exosphere. J. Geophys. Res. 111 (A07207). https://doi.org/10.1029/2005JA011364.

Witze, A., 2021. Will increasing traffic to the Moon contaminate its precious ice? Nature 589, 180–181. https://doi.org/10.1038/d41586-020-03262-9.

Wurz, P., Fatemi, S., Galli, A., et al., 2022. Particles and photons as drivers for particle release from the surfaces of the Moon and Mercury. Space Sci. Rev. 218 (10). https://doi.org/10.1007/s11214-022-00875-6.

Wurz, P., Rohner, U., Whitby, J.A., et al., 2007. The lunar exosphere: The sputtering contribution. Icarus 191, 486–496. https://doi.org/10.1016/j.icarus.2007.04.034.

Yokota, S. et al., 2009. First direct detection of ions originating from the Moon by MAP-PACE IMA onboard SELENE (KAGUYA). Geophys. Res. Lett., 36(L11201). doi:10.1029/2009GL038185.

Zhang, H., Khurana, K.K., Kivelson, M.G., et al., 2014. Three-dimensional lunar wake reconstructed from ARTEMIS data. J. Geophys. Res.: Space. Physics 119, 5220–5243. https://doi.org/10.1002/2014JA020111.